# Nondiffusive electron transport in metals: A two-temperature Boltzmann transport equation analysis of thermoreflectance experiments

Justin P. Freedman, Robert F. Davis, and Jonathan A. Malen

Phys. Rev. B **99**, 054308 — Published 27 February 2019

DOI: 10.1103/PhysRevB.99.054308

# Nondiffusive electron transport in metals interpreted by a two-temperature Boltzmann transport equation analysis of thermoreflectance experiments

Justin P. Freedman[1], Robert F. Davis[1], and Jonathan A. Malen[1,2,a)]

[1] *Department of Materials Science and Engineering, Carnegie Mellon University, Pittsburgh, PA 15213 USA*
[2] *Department of Mechanical Engineering, Carnegie Mellon University, Pittsburgh, PA 15213 USA*

[a)] Author to whom correspondence should be addressed. Electronic mail: jonmalen@andrew.cmu.edu.

We develop a theoretical framework based on the electron-phonon coupled Boltzmann transport equations (BTEs) for the interpretation of nondiffusive thermal conductivity measurements in metals made via frequency domain thermoreflectance (FDTR). The thermal conductivity of a bulk gold crystal was measured over a temperature range of 23 K to 304 K as a function of FDTR's laser spot size. Our interpretation of these measurements by a two-temperature heat diffusion model finds that the thermal conductivity is suppressed when the laser spot size is comparable to electron mean free paths. Using a simplified spherical geometry that enables analytical solutions, we compare the two-temperature diffusion model with the coupled BTEs, to identify a thermal conductivity suppression function. We also conclude that over the timescales of our experiment electron-phonon nonequilibrium is negligible, but that the length scale of heat deposition by hot electrons critically influences our interpretation.

## I. INTRODUCTION

Thermal transport in materials is commonly described by diffusive laws that assume that the energy carrier mean free paths (MFPs) are much smaller than the length scales of interest. As the length scales of interest decrease and become commensurate to the material's thermal energy carrier MFPs, diffusive laws break down. Novel, laser-based thermal conductivity ($k$) measurement techniques, such as broadband frequency domain thermoreflectance (BB-FDTR) [1,2], transient thermal grating (TTG) [3], and time domain thermoreflectance (TDTR) [4-6], have demonstrated this phenomenon, known as nondiffusive thermal transport, in dielectric materials, where phonons are the lone carriers of heat. In these studies, as the experimental length scales (laser spot size radius ($r_0$) and thermal penetration depth ($L_P$) in BB-FDTR and TDTR, length of the grating period ($L_G$) in TTG) become comparable to the MFPs of select phonons, the application of the heat diffusion equation results in apparent values of $k$ that are suppressed from the bulk value.

Two fundamental energy carriers exist in a metal; electrons and phonons. Electrons dominate $k$ in metals, while phonons are primarily responsible for the volumetric heat capacity ($C$) [7]. Thermal nonequilibrium between electrons and phonons results in the exchange of energy between the two energy carriers in a process known as electron-phonon coupling [8-11]. The length scales associated with electron-phonon coupling differ from the MFPs of electrons and phonons in a metal. Therefore, unlike in dielectrics, where a single material length scale can be compared to the experimental length scales ($r_0$, $L_P$, or $L_G$), multiple material length scales must be considered in a metal.

The thermal conductivity of electrons in a metal is described by the equation $k_e = \int_0^\infty k_{\Lambda_e} \, d\Lambda_e = \frac{1}{3} C_e v_e \Lambda_e$, where $k_e$ is the bulk electronic thermal conductivity in a metal, $k_\Lambda$ is the electron contribution to thermal conductivity per unit MFP, $C_e$ is the volumetric heat capacity of the electron, $v_e$ is the Fermi velocity, and $\Lambda_e$ is the electron MFP in a metal. In metals, a gray electron MFP is an appropriate approximation [7]. Therefore, the thermal conductivity accumulation function [12], $k_{accum}$, for electrons in a metal can be written as a step function with the form

$$k_{accum}\left(\Lambda_e^*\right) = \begin{cases} k_e, \Lambda_e^* \geq \Lambda_e \\ 0, \Lambda_e^* < \Lambda_e \end{cases}. \tag{1}$$

The relationship between an energy carrier's MFP and its contribution to the measured value of thermal conductivity, $k_{exp}$, in a FDTR experiment is defined as [13]

$$k_{\exp}\left(r_0, L_P\right) = \int_0^\infty S\left(\Lambda, r_0, L_P\right) k_\Lambda d\Lambda, \tag{2}$$

where $S$ is the thermal conductivity suppression function. Using the $k_{accum}$ for electrons in Equation (1), $k_{exp}$ in a metal can be written as

$$k_{\exp}\left(r_0, L_P\right) = S\left(\Lambda_e, r_0, L_P\right) k_e. \tag{3}$$

To date, $S$ has been theoretically derived based on comparisons to the diffusive thermal transport equation and the Boltzmann transport equation (BTE) for dielectric materials measured via BB-FDTR [14], TDTR [6], and TTG [15,16].

In this study, we derive $S$ for a metal measured via FDTR based on an analytical solution to the two-temperature BTE in spherical coordinates. The timescales of electron-phonon coupling are less than 1 ps for temperatures between 10 K and 300 K [17], while the timescales of FDTR range from 0.2 μs and 10 μs for the modulation frequencies used

here (5 MHz to 100 kHz). Hence, FDTR is not typically sensitive to non-equilibria of the energy carriers under these conditions. We herein consider how electron-phonon coupling length scales and $\Lambda$ of electrons and phonons relative to the $r_0$, influence this assumption. To resolve these effects the BTE solution is compared with the solution to the two-temperature diffusive model to explain how nondiffusive electron transport can be interpreted as a suppressed value of $k$. We show that FDTR measurements of a bulk gold (Au) crystal, interpreted via the coupled heat diffusion equations with the ability to exponentially deposit heat within the Au, deviate from the bulk values of $k$ when $r_0$ is comparable to $\Lambda_e$. Au was chosen for our experiments because of its weak electron-phonon coupling [18,19] and long $\Lambda_e$ that enable nondiffusive behavior at experimentally attainable temperatures. By examining the BTE and diffusive equation's predicted thermal resistances at the surface of Au as a function of $r_0$ we also demonstrate that nondiffusive and nonequilibrium thermal transport processes can be separated and their onsets identified.

## II. GEOMETRY AND BOUNDARY CONDITIONS FOR THE BTE AND HEAT DIFFUSION EQUATIONS

Thermal transport in metals is often described by a two-temperature model that separates the electrons and phonons into two effective temperatures; $T_e(r)$ for electrons and $T_p(r)$ for phonons [20]. Here, the effective temperatures are functions of position in the metal, $r$. The electrons and phonons exchange energy at a rate per unit volume, $q'''_{e-p}(r)$, that is proportional to the difference in effective temperatures, such that $q'''_{e-p}(r) = g\left[T_e(r) - T_p(r)\right]$, where $g$ is a proportionality constant known as the electron-phonon coupling parameter. No heating frequency dependence on $k_{exp}$ was observed over

the range of heating frequencies used in the FDTR experiment presented later (100 kHz to 5 MHz). At low temperatures, where nondiffusive behavior was observed, $L_P$ varied between ~93 μm and ~13 μm, which are greater than the values of $r_0$ used in the FDTR experiment. Therefore, to simplify our analysis time-independent solutions to the BTE and heat diffusion equations are presented.

To accurately model the FDTR geometry for the purposes of fitting our experimental data a solution to the heat diffusion model in the two-dimensional cylindrical coordinate system is used in Section VI. An analytical solution to the BTE in this geometry is, however, impossible so we consider simple analytical solutions in the one-dimensional spherical geometry. By using spherical symmetry, rather than a planar Cartesian system, we introduce a spatial dimension–sphere radius ($r_0$)–that can be likened to spot size radius, as shown in Figure 1. Regner *et al* [14] demonstrated that a spherical geometry can estimate the effects of a finite $1/e^2$ laser spot size in FDTR and found that the analytical results compared favorably with experimental data, yet it has not been rigorously proven to approximate the true geometry.

In a FDTR measurement photons from the pump laser are absorbed volumetrically with exponential temperature decay from the surface. The absorbed heat flux excites the metal's electrons, producing a temperature rise in $T_e$. Previous studies have shown that the excited electrons diffuse and thermalize with the phonons with exponential decay over the length scale $L_{th} = \sqrt{\frac{k_e C_p}{g\left(C_p + C_e\right)}} \approx \sqrt{\frac{k_e}{g}}$, where $L_{th}$ is the thermalization length and $C_p$ is the phonon volumetric heat capacity (in metals $C_e << C_p$) [8,21]. A realistic depiction of exponential spatial absorption makes an analytical solution to the BTE and

heat diffusion equation intractable. Instead, we model an isothermal region of thickness $L_{th}$, where $T_e$ and $T_p$ are distinct and spatially homogenous. Notably, the $S$ determined in Section V is independent of the value of $L_{th}$ chosen because identical treatment is used in both the BTE and heat diffusion equation. The rise in $T_e$ produces a temperature difference between the electrons and phonons in the isothermal region ($r_0 - L_{th} < r < r_0$), inducing a heat flux from the electrons to the phonons. The net heat flux from the electrons to the phonons within the isothermal region is quantified by $q'''_{e-p}$ integrated over the thickness $L_{th}$, which equals $gL_{th}\left(T_e - T_p\right)$.

Our solution domain extends from $r = r_0$ to $r \to \infty$. The exchange of thermal energy from the electrons to the phonons within $r_0 - L_{th} < r < r_0$ results in heating of the solution domain. The magnitude of the electron and phonon heat fluxes at $r = r_0$ are

$$q_e\big|_{r=r_0} = q_0 - gL_{th}\left(T_e - T_p\right), \tag{4}$$

$$q_p\big|_{r=r_0} = gL_{th}\left(T_e - T_p\right), \tag{5}$$

where $q_0$ is the magnitude of the absorbed laser heat flux. Notably, $T_e$ and $T_p$ do not represent absolute temperatures, but rather perturbations from the ambient temperature, which is assumed to equal zero for convenience, causing

$$T_e\big|_{r\to\infty} = 0, \tag{6}$$

$$T_p\big|_{r\to\infty} = 0. \tag{7}$$

## III. ELECTRON AND PHONON TEMPERATURES

### A. Two-temperature spherical heat diffusion equations

The coupled time-independent two-temperature heat diffusion equations in spherical coordinates, where temperature gradients occur only in the radial direction, are

$$0 = \frac{1}{r^2}\frac{d}{dr}\left( k_e r^2 \frac{dT_{diff,e}}{dr} \right) - g\left( T_{diff,e} - T_{diff,p} \right), \tag{8}$$

$$0 = \frac{1}{r^2}\frac{d}{dr}\left( k_p r^2 \frac{dT_{diff,p}}{\partial r} \right) + g\left( T_{diff,e} - T_{diff,p} \right), \tag{9}$$

where $k_p$ is the phonon thermal conductivity in a metal. Here, $T_{diff,e}$ and $T_{diff,p}$ are the effective electron and phonon temperatures of the material that result from our solution to the coupled heat diffusion equations. Substituting the relations $T_{diff,e} = \frac{\theta_{diff,e}}{r}$ and $T_{diff,p} = \frac{\theta_{diff,p}}{r}$ into Equations (8) and (9) leads to

$$\frac{d^2\theta_{diff,e}}{dr^2} = \frac{g}{k_e}\theta_{diff,e} - \frac{g}{k_e}\theta_{diff,p}, \tag{10}$$

$$\frac{d^2\theta_{diff,p}}{dr^2} = -\frac{g}{k_p}\theta_{diff,e} + \frac{g}{k_p}\theta_{diff,p}. \tag{11}$$

The boundary conditions outlined in Equations (4) and (5) lead to

$$q_e\big|_{r=r_0} = -k_e \frac{dT_{diff,e}}{dr}\bigg|_{r=r_0} = q_0 - gL_{th}\left[ T_{diff,e}(r_0) - T_{diff,p}(r_0) \right], \tag{12}$$

$$q_p\big|_{r=r_0} = -k_p \frac{dT_{diff,p}}{dr}\bigg|_{r=r_0} = gL_{th}\left[ T_{diff,e}(r_0) - T_{diff,p}(r_0) \right]. \tag{13}$$

Figure 1(a) shows the spherical approximation of a metal in a FDTR experiment based on the heat diffusion equations and the corresponding boundary conditions. Solving Equations (10) and (11), the effective temperatures can be expressed as

$$T_{diff,e}(r)=\frac{q_0}{r(AF+BD)}\left[B+A(\gamma-L_e)e^{(r_0-r)/L_e}\right], \tag{14}$$

$$T_{diff,p}(r)=\frac{q_0}{r(AF+BD)}\left[B-AL_e e^{(r_0-r)/L_e}\right], \tag{15}$$

where $\gamma=\sqrt{\frac{k_e k_p+k_p^2}{gk_e}}$, $L_e=\sqrt{\frac{1}{\frac{g}{k_e}+\frac{g}{k_p}}}$, $A=\frac{k_p}{r_0^2}$, $D=\frac{k_e}{r_0^2}$, $B=\frac{1}{r_0}\left(gL_{th}\gamma+k_p\left(\frac{L_e}{r_0}+1\right)\right)$,

and $F=\frac{1}{r_0}\left(gL_{th}\gamma+k_e\left(\frac{\gamma-L_e}{r_0}+\frac{\gamma}{L_e}-1\right)\right)$.

Examining Equations (14) and (15), the onset of nonequilibrium between the electrons and phonons in a FDTR experiment can be identified. In a FDTR experiment, the temperature to heat flux is probed at the surface of the material. Assuming $k_e >> k_p$, the difference in the electron and phonon temperatures predicted by the heat diffusion equations at the surface of the sphere, $r = r_0$, is

$$T_{diff,e}(r_0)-T_{diff,p}(r_0)\approx\frac{q_0/k_e}{\frac{L_{th}}{L_e^2}+\frac{1}{r_0}}\approx\frac{q_0/k_e}{\frac{\sqrt{k_e g}}{k_p}+\frac{1}{r_0}}. \tag{16}$$

When $r_0 >> \frac{k_p}{\sqrt{gk_e}}$ the difference between $T_{diff,e}$ and $T_{diff,p}$ is independent of $r_0$ and small at the surface. When $r_0 \approx \frac{k_p}{\sqrt{gk_e}}$ $T_{diff,e}$ and $T_{diff,p}$ diverge and electron-phonon nonequilibrium increases. Therefore, the onset of electron-phonon nonequilibrium in a metal measured via FDTR under low heating frequency conditions occurs when $r_0 \approx$

$L_{\text{noneq}}$, where $L_{noneq} = \dfrac{k_p}{\sqrt{gk_e}}$. In materials where only one energy carrier exists, such as dielectrics, $g \to \infty$ causing $L_{\text{noneq}} = 0$.

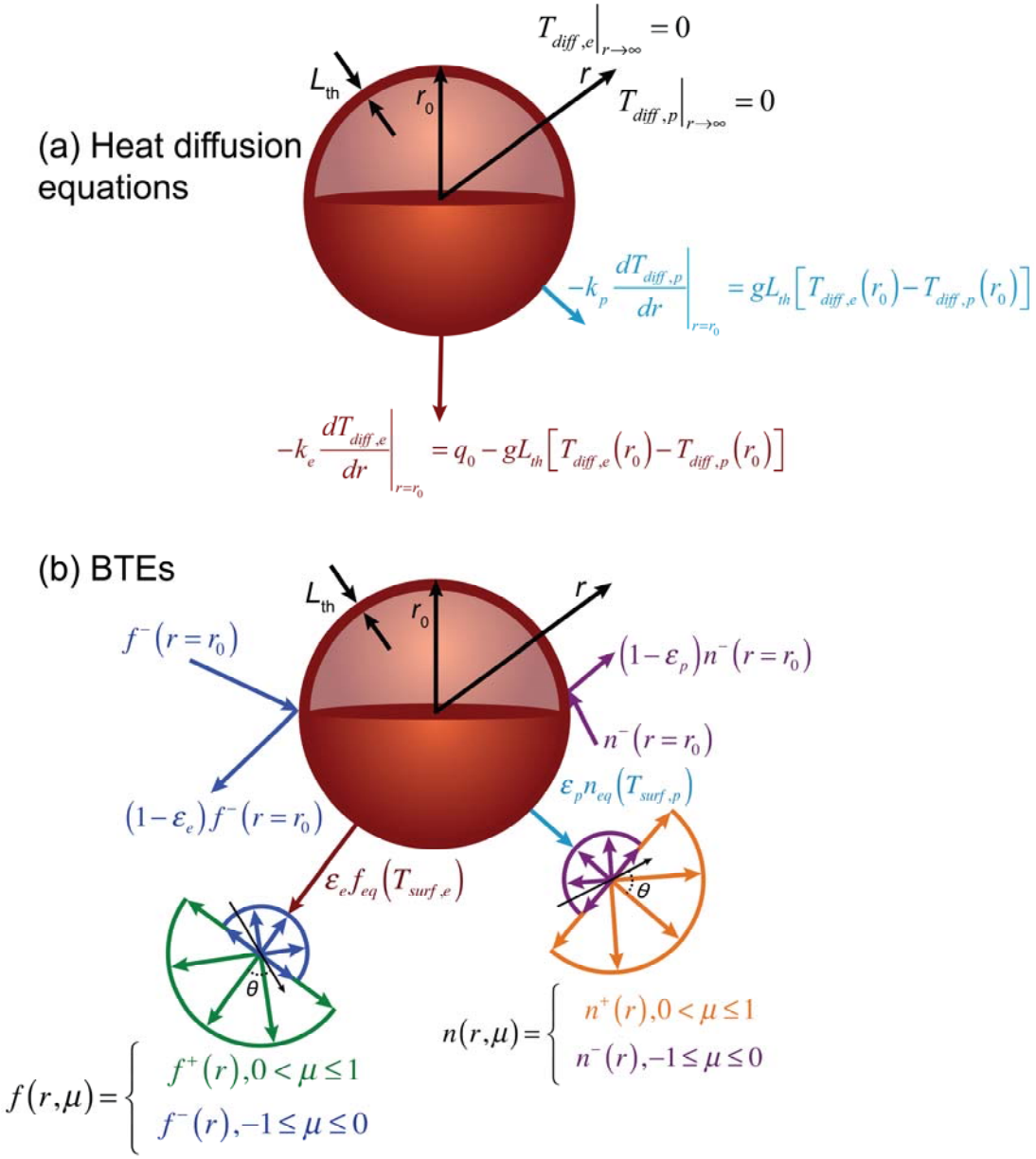


FIG. 1. Spherical approximation of a metal in a FDTR experiment. (a) Boundary conditions based on the two-temperature heat diffusion equations. (b) Boundary conditions based on the two-temperature BTEs, where the

energy carriers moving in the negative *r*-direction either become fully thermalized upon entering the isothermal region ($\varepsilon \approx 0$), $r_0 - L_{th} < r < r_0$, or scatter elastically at the physical boundary ($\varepsilon \approx 1$).

**B. Two-temperature spherical Boltzmann transport equations**

A solution to the two-temperature spherical BTE is now derived assuming the relaxation time approximation, gray approximations for electron and phonon relaxation times, and the $P_1$ approximation to eliminate the angular dependence of energy carriers. The 1-D time-independent BTE under the relaxation time approximation in spherical coordinates for a single gray thermal energy carrier system is [14]

$$\mu \frac{\partial w}{\partial r} + \frac{1-\mu^2}{r} \frac{\partial w}{\partial \mu} = \frac{w_{eq} - w}{\tau v} + Q, \tag{17}$$

where $w$ is the energy density per unit solid angle, also known as the distribution function, $w_{eq}$ is the equilibrium distribution function, $v$ is the velocity of the energy carrier, $\mu$ is the directional cosine that accounts for the velocity of energy carriers traveling at different angles from the *r*-direction, $\tau$ is the energy carrier lifetime, and $Q$ is a source term. The distribution functions for electrons ($f$) and phonons ($n$) are defined as [22]

$$f(r,\mu) = \frac{1}{4\pi} \int (E - E_F) D_e(E) f_{pop}(r,\mu) dE, \tag{18}$$

$$n(r,\mu) = \frac{1}{4\pi} \sum_P \int \hbar \omega D_p(\omega) n_{pop}(r,\mu) d\omega, \tag{19}$$

where $f_{pop}$ and $n_{pop}$ are the electron and phonon occupation functions, $E$ is the energy of an electron, $E_F$ is the Fermi energy of the metal, $\omega$ is the frequency of a phonon, $D_e$ is the electron density of states per unit energy, $D_p$ is the phonon density of states per unit

frequency, and $\hbar$ is the reduced Planck constant. In an electron-phonon coupled system the source term is $Q = \frac{g}{4\pi v}\left(T_e - T_p\right)$. Here, $Q$ represents the energy density per unit length per unit solid angle exchanged between the electrons and phonons. Regner *et al* [14] recently solved the BTE in Equation (17) on a per mode level, where $Q$ = 0, while our definitions of $f$ and $n$ in Equations (18) and (19) are integrated over all modes. This is because the electron-phonon coupling constant is not experimentally known on a per mode basis, while the total electron-phonon coupling constant integrated over all modes, $g$, is well known in select metals [23,24]. Using Equations (19) and (20), and assuming no external electric field is applied to the metal, the time-independent, electron-phonon coupled, gray, spherical BTEs under the relaxation time approximation are [22]

$$\mu\frac{\partial f}{\partial r} + \frac{1-\mu^2}{r}\frac{\partial f}{\partial \mu} = \frac{f_{eq} - f}{\tau_e v_e} - \frac{g}{4\pi v_e}\left(T_{BTE,e} - T_{BTE,p}\right), \tag{20}$$

$$\mu\frac{\partial n}{\partial r} + \frac{1-\mu^2}{r}\frac{\partial n}{\partial \mu} = \frac{n_{eq} - n}{\tau_p v_p} + \frac{g}{4\pi v_p}\left(T_{BTE,e} - T_{BTE,p}\right), \tag{21}$$

where $f_{\text{eq}}$ and $n_{\text{eq}}$ are the equilibrium electron and phonon distribution functions, $\tau_e$ and $\tau_p$ are the electron and phonon relaxation times, and $T_{\text{BTE,e}}$ and $T_{\text{BTE,p}}$ are the effective electron and phonon temperatures that result from our solution to the two-temperature BTEs. The equilibrium distributions, $f_{\text{eq}}$ and $n_{\text{eq}}$, are defined by Equations (18) and (19), where $f_{\text{pop}}$ and $n_{\text{pop}}$ are the Fermi-Dirac ($f_{\text{FD}}$) and Bose-Einstein ($n_{\text{BE}}$) distributions. For small perturbations from the ambient temperature, $f_{FD} = \frac{df_{FD}}{dT_{BTE,e}} T_{BTE,e}$ and $n_{BE} = \frac{dn_{BE}}{dT_{BTE,p}} T_{BTE,p}$, such that [15]

$$T_{BTE,e} = \frac{4\pi f_{eq}}{C_e}, \tag{22}$$

$$T_{BTE,p} = \frac{4\pi n_{eq}}{C_p}. \tag{23}$$

An analytical solution to the spherical BTE for a single energy carrier system in a gray medium was outlined by Regner *et al* [14] using the method of spherical harmonics under the $P_1$ approximation [25], which eliminates the $\mu$-dependence from Equation (17). Using a similar approach to Regner *et al* [14], Equations (20) and (21) under the $P_1$ approximation [25] lead to a system of four first-order differential equations

$$\frac{df_1}{dr} + \frac{2}{r} f_1 + \frac{g}{v_e C_e} f_0 - \frac{g}{v_e C_p} n_0 = 0, \tag{24}$$

$$\frac{df_0}{dr} + \frac{3}{\tau_e v_e} f_1 = 0, \tag{25}$$

$$\frac{dn_1}{dr} + \frac{2}{r} n_1 + \frac{g}{v_p C_p} n_0 - \frac{g}{v_p C_e} f_0 = 0, \tag{26}$$

$$\frac{dn_0}{dr} + \frac{3}{\tau_p v_p} n_1 = 0, \tag{27}$$

where $f_1$ and $f_0$ represent the 1st and 0th electron distribution moments and $n_1$ and $n_0$ represent the 1st and 0th phonon distribution moments. The effective temperatures of the electrons and phonons within the metal are proportional to the 0th distribution moments, defined as a linear combination of energy carriers moving in the positive (+) and negative (-) directions, such that $f_0 = 2\pi\left(f^+ + f^-\right)$ and $n_0 = 2\pi\left(n^+ + n^-\right)$ [25]. The heat flux of the electrons and phonons are proportional to the 1st distribution moments, where $f_1 = \pi\left(f^+ - f^-\right)$ and $n_1 = \pi\left(n^+ - n^-\right)$ [25]. The distribution functions, $f^+$, $f^-$, $n^+$, and

$n^-$ are hemispherically isotropic, as shown in Figure 1(b), where $f^+(r) = f(r, 0 < \mu \le 1)$, $f^-(r) = f(r, -1 \le \mu \le 0)$, $n^+(r) = n(r, 0 < \mu \le 1)$, and $n^-(r) = n(r, -1 \le \mu \le 0)$ [25]. The equilibrium distribution functions are defined as the average of energy carriers moving in the positive and negative directions and are therefore related to the 0th distribution moments as $f_{eq} = \frac{\left(f^+ + f^-\right)}{2} = \frac{f_0}{4\pi}$ and $n_{eq} = \frac{\left(n^+ + n^-\right)}{2} = \frac{n_0}{4\pi}$.

At $r = r_0$, which is one $L_{th}$ from the surface, we assume that there is a black surface that emits and absorbs electrons and phonons that emerge into the bulk of the Au at the temperature of the isothermal region, $r_0$ - $L_{th}$ < $r$ < $r_0$ [26]. Since no physical or thermal boundary exists for the electrons and phonons at $r = r_0$, the emissivity of the electrons and phonons depend on whether they scatter and equilibrate within the isothermal region. This is related to the temperature dependent ratio of $L_{th}$ to $\Lambda_e$.

Figure 2 shows previously reported temperature dependent values of $L_{th}$, $\Lambda_e$ (gray), $\Lambda_p$ (gray), and $L_{noneq}$ based on $k$ measurements of Au. The electron MFP based on electrical resistivity measurements of Au, $\Lambda_{e,elec} = \frac{m v_e}{\eta q^2 \rho}$, is also included in Figure 2 ($m$ is the mass of an electron, $\eta$ is the free electron density, $q$ is the electronic charge, and $\rho$ is the electrical resistivity). The temperature dependent $k$ data was found in Ref. [27]. To determine $\Lambda_p$, the values of $k_p$ found in Ref. [28] were used, but were not shown for temperatures below 60 K. Therefore, for temperatures below 60 K, the values of $k_p$ were extrapolated using the Born-von-Karman Slack (BvKS) model [29]. Although the BvKS model does not account for electron-phonon scattering, the spherical BTE and diffusive models are not highly sensitive to increases or decreases in $k_p$ by a factor of 3. The

temperature-dependent values of $g$ and $C_p$ were found in Refs. [18] and [30], respectively, while $C_e = \chi T$, where $\chi$ = 67.6 J m$^{-3}$ K$^{-2}$ (Ref. [23]). The velocities of the electrons and phonons were assumed to be temperature-independent, where $v_e$ = 1400 km s$^{-1}$ and $v_p$ = 3240 m s$^{-1}$ [31,32]. The electrical resistivity of Au was determined using Data Set 15 in Ref. [33].

It is shown in Figure 2, that for temperatures above 90 K $\Lambda_e > L_{th}$. In this temperature range the electrons scatter multiple times before they reach thermal equilibrium with the phonons. Here, thermal transport in the metal can be described by conventional parabolic heat conduction. At temperatures below 90 K, $\Lambda_e > L_{th}$. Qiu and Tien [34] also observed this for temperatures below 50 K when comparing electron relaxation times and electron-phonon thermalization times in Au, copper, and silver and explained this phenomenon as hyperbolic heat conduction. Prior data clearly indicates that under certain conditions electrons can have mean free paths longer than the length scales associated with thermal equilibration.

To simplify our analysis we make the approximation that when $L_{th} > \Lambda$, the energy carrier moving in the negative direction enters the isothermal region, scatters before or after striking the physical surface of the metal and thermalizes within the isothermal region. In this case, the effective emissivity of the artificial boundary at $r_0$ is equivalent to one. On the other hand, when $L_{th} < \Lambda$ (temperatures below 90 K in Au, as shown in Figure 2) the energy carrier moving in the negative direction enters and traverses the entire length of the isothermal region, scatters elastically at the surface of the material, and travels unimpeded across the isothermal layer back into the bulk region. In this case, most of the energy carriers will not thermalize within the isothermal region and exit the

region with the same energy that they entered with. This is equivalent to an energy carrier reflecting at the $r = r_0$ boundary. Therefore, the emissivity of the artificial boundary at $r = r_0$ is roughly equal to zero. Under this approximation, the equilibrium electron and phonon temperatures in the isothermal region ($T_{\text{surf,e}}$ and $T_{\text{surf,p}}$) are defined as [26]

$$f^{+}\left(r_0\right) = \varepsilon_e \frac{C_e T_{surf,e}}{4\pi} + \left(1-\varepsilon_e\right) f^{-}\left(r_0\right), \begin{cases} \varepsilon_e \approx 1, T > 90K \\ \varepsilon_e \approx 0, T < 90K \end{cases}, \tag{28}$$

$$n^{+}\left(r_0\right) = \varepsilon_p \frac{C_p T_{surf,p}}{4\pi} + \left(1-\varepsilon_p\right) n^{-}\left(r_0\right), \varepsilon_p \approx 1, \tag{29}$$

where $\varepsilon_{\text{e}}$ and $\varepsilon_{\text{p}}$ are the electron and phonon emissivities at $r = r_0$ and $T_{\text{surf,e}}$ and $T_{\text{surf,p}}$ are the surface temperatures relevant to FDTR. The surface temperatures can be written in terms of $f_1$, $f_0$, $n_1$, and $n_0$ as

$$T_{surf,e} = \frac{f_0\left(r_0\right)}{C_e} + \frac{\left(4-2\varepsilon_e\right) f_1\left(r_0\right)}{C_e \varepsilon_e}, \tag{30}$$

$$T_{surf,p} = \frac{n_0\left(r_0\right)}{C_p} + \frac{\left(4-2\varepsilon_p\right) n_1\left(r_0\right)}{C_p \varepsilon_p}. \tag{31}$$

Using Equations (30) and (31) to define the electron and phonon temperatures at the surface of the material, the boundary conditions in Equations (4) and (5) become

$$q_e\big|_{r=r_0} = v_e f_1\left(r_0\right) = q_0 - gL_{th}\left(T_{surf,e} - T_{surf,p}\right), \tag{32}$$

$$q_p\big|_{r=r_0} = v_p n_1\left(r_0\right) = gL_{th}\left(T_{surf,e} - T_{surf,p}\right), \tag{33}$$

where the electron and phonon heat fluxes are equal to their respective 1st distribution moments multiplied by group velocity. Applying the boundary conditions in Equations (6), (7), (32), and (33) and solving Equations (24)-(27), the electron and phonon 0th and 1st distribution moments are

$$f_0(r)=\begin{cases}\dfrac{q_0}{r\left((H-U)(J+Z)+(M+Y)(K+W)\right)}\left(\dfrac{C_e(K+W)}{C_p}+(H-U)\beta\psi\right), r=r_0\\ \dfrac{q_0}{r(HJ+MK)}\left(\dfrac{C_eK}{C_p}+H\beta\psi e^{(r_0-r)/\alpha\psi}\right), r>r_0\end{cases}, \tag{34}$$

$$n_0(r)=\begin{cases}\dfrac{q_0}{r\left((H-U)(J+Z)+(M+Y)(K+W)\right)}\left((K+W)-(H-U)\alpha\psi\right), r=r_0\\ \dfrac{q_0}{r(HJ+MK)}\left(K-H\alpha\psi e^{(r_0-r)/\alpha\psi}\right), r>r_0\end{cases}, \tag{35}$$

$$f_1(r)=\begin{cases}\dfrac{q_o\tau_e v_e}{3r^2\left((H-U)(J+Z)+(M+Y)(K+W)\right)}\left(\dfrac{C_e(K+W)}{C_p}+(H-U)\beta\left(\psi+\dfrac{r}{\alpha}\right)\right), r=r_0\\ \dfrac{q_o\tau_e v_e}{3r^2(HJ+KM)}\left(\dfrac{C_eK}{C_p}+H\beta\left(\psi+\dfrac{r}{\alpha}\right)e^{(r_0-r)/\alpha\psi}\right), r>r_0\end{cases}, \tag{36}$$

$$n_1(r)=\begin{cases}\dfrac{q_0\tau_p v_p}{3r^2\left((H-U)(J+Z)+(M+Y)(K+W)\right)}\left((K+W)-(H-U)(\alpha\psi+r)\right), r=r_0\\ \dfrac{q_0\tau_p v_p}{3r^2(HJ+KM)}\left(K-H(\alpha\psi+r)e^{(r_0-r)/\alpha\psi}\right), r>r_0\end{cases}, \tag{37}$$

where $\psi=\sqrt{\dfrac{1}{3g\left(C_e\tau_e v_e^2+C_p\tau_p v_p^2\right)}}$, $\beta=\sqrt{\dfrac{C_eC_p\tau_p^3v_p^6}{\tau_e v_e^2}}$, $\alpha=\sqrt{C_eC_p\tau_e\tau_p v_e^2v_p^2}$,

$$\lambda_e=\frac{\tau_e v_e\left(4-2\varepsilon_e\right)}{\varepsilon_e},\ \lambda_p=\frac{\tau_p v_p\left(4-2\varepsilon_p\right)}{\varepsilon_p},\ H=\frac{\tau_p v_p^2}{3r_0^2}, U=\frac{gL_{th}}{3r_0^2C_p}\left(\lambda_e-\lambda_p\right),$$

$$K=\frac{1}{3r_0^2}\left(\tau_p v_p^2(\alpha\psi+r_0)+3gL_{th}\psi r_0\left(\frac{\beta}{C_e}+\frac{\alpha}{C_p}\right)\right), W=\frac{gL_{th}}{3r_0^2}\left(\frac{\lambda_e\beta}{C_e}\left(\psi+\frac{r_0}{\alpha}\right)+\frac{\lambda_p}{C_p}(\alpha\psi+r_0)\right),$$

$$M=\frac{\tau_e v_e^2C_e}{3r_0^2C_p},\ Y=\frac{gL_{th}}{3r_0^2C_p}\left(\lambda_e-\lambda_p\right),\ J=\frac{1}{3r_0^2}\left(\tau_e v_e^2\beta\left(\psi+\frac{r_0}{\alpha}\right)+3gL_{th}\psi r_0\left(\frac{\beta}{C_e}+\frac{\alpha}{C_p}\right)\right),$$

$$Z=\frac{gL_{th}}{3r_0^2}\left(\frac{\lambda_e\beta}{C_e}\left(\psi+\frac{r_0}{\alpha}\right)+\frac{\lambda_p}{C_p}(\alpha\psi+r_0)\right).$$

Under the gray approximation, where $k_e = \frac{1}{3} C_e v^2{}_e \tau_e$ and $k_p = \frac{1}{3} C_p v_p^2 \tau_p$, the spatial decay length in the BTE is $\alpha\psi = L_e$. Therefore, both the diffusive and BTE temperatures exponentially decay over the same length, $L_e$, in the time-independent, gray solution.

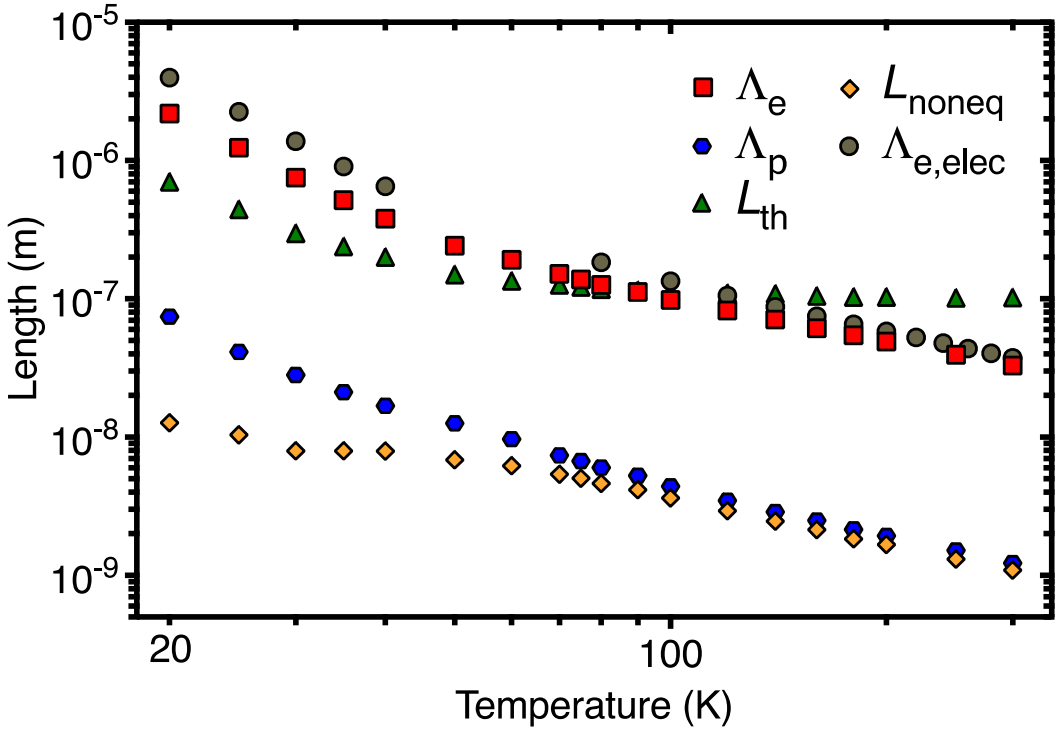


FIG. 2. $L_{th}$, $\Lambda_e$ (gray), $\Lambda_p$ (gray), $L_{noneq}$, and $\Lambda_{e,elec}$ in a bulk Au crystal plotted over a temperature range of 20 K to 300 K. The values of $\Lambda_e$ and $\Lambda_{e,elec}$ are approximately the same over the entire temperature range. For temperatures below 90 K $L_{th}$ is shorter than $\Lambda_e$, suggesting hyperbolic heat conduction.

## IV. ELECTRON AND PHONON SURFACE THERMAL RESISTANCES AS A FUNCTION OF $r_0$

In a FDTR experiment $k_{\text{exp}}$ is a function of the measured thermal resistance at the surface of a material and the predicted thermal resistance is typically based on a diffusive model. For the nondiffusive regime the measured thermal resistances at the surface of a metal more aptly are based on the BTE temperatures, where

$$R_{BTE,e} = \frac{T_{surf,e}}{q_0}, \tag{38}$$

$$R_{BTE,p} = \frac{T_{surf,p}}{q_0}, \tag{39}$$

while the two-temperature diffusive thermal resistances are

$$R_{diff,e} = \frac{T_{diff,e}\left(r_0\right)}{q_0}, \tag{40}$$

$$R_{diff,p} = \frac{T_{diff,p}\left(r_0\right)}{q_0}. \tag{41}$$

In Figures 3(a) and 3(b) $R_{\text{BTE,e}}$, $R_{\text{BTE,p}}$, $R_{\text{diff,e}}$, and $R_{\text{diff,p}}$ for a bulk Au crystal are plotted as a function of $r_0$. The ambient temperatures are 300 K and 25 K in Figures 3(a) and 3(b), respectively. At 300 K, both $\Lambda_{\text{e}}$ and $\Lambda_{\text{p}}$ are much less than $L_{\text{th}}$. Therefore, $\varepsilon_e = 1$ and $\varepsilon_p = 1$ since the two energy carriers enter the isothermal layer unimpeded from the bulk region and thermalize within the layer. At 25 K, $\Lambda_{\text{e}} > L_{\text{th}}$ and $\Lambda_{\text{p}} < L_{\text{th}}$, which implies that $\varepsilon_e = 0$ and $\varepsilon_p = 1$. Since an emissivity of zero cannot be used in Equations (30) and (31), a value of $\varepsilon_e = 0.01$ was used instead. Notably, the BTE thermal resistances were unchanged when $\varepsilon_e = 10^{-2}$, $\varepsilon_e = 10^{-7}$, and $\varepsilon_e = 10^{-15}$.

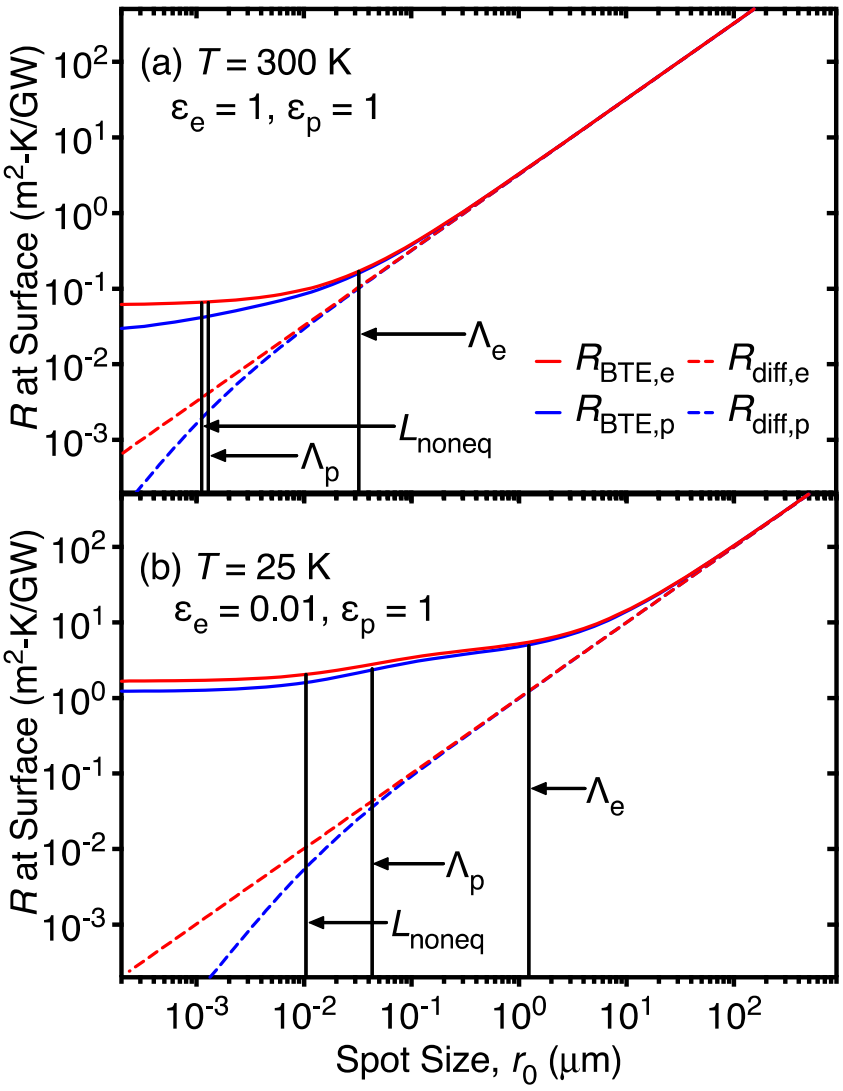


FIG. 3. Electron and phonon thermal resistances at the surface of a bulk Au crystal based on the two-temperature, spherical BTE and the two-temperature, spherical diffusive equations plotted as a function of $r_0$. The material length scales, $\Lambda_e$, $\Lambda_p$, and $L_{noneq}$, are indicated with black vertical lines to highlight the behavior of the thermal resistance profiles as $r_0$ becomes commensurate to them. (a) The ambient temperature is 300 K, where $\varepsilon_e = 1$ and $\varepsilon_p = 1$. (b) The ambient temperature is 25 K, where $\varepsilon_e = 0.01$ and $\varepsilon_p = 1$.

When $r_0 >> \Lambda_e$ and $\Lambda_p$ in Figure 3, $R_{BTE}$ and $R_{diff}$ are equivalent. Here, electrons and phonons are in thermal equilibrium and the transport processes are purely diffusive. In this regime the thermal resistances of the electrons and phonons can be accurately described by the heat diffusion equations. As $r_0$ becomes commensurate to $\Lambda_e$ (the longer of the two MFPs) $R_{BTE,e}$ and $R_{BTE,p}$ diverge from $R_{diff,e}$ and $R_{diff,p}$. This is because the electrons transport nondiffusively through the characteristic length scale, $r_0$. The coupled heat diffusion equations assume that the energy carrier MFPs are much smaller than $r_0$ and cannot accurately describe the thermal transport processes in this regime. Interestingly, even though $r_0 >> \Lambda_p$ the phonons exhibit nondiffusive transport in this regime due to the coupled behavior of the energy carriers. As the laser spot size decreases and $r_0 \approx \Lambda_p$ (the shorter of the two MFPs), the difference between the two BTE thermal resistances remains constant with decreasing $r_0$. Based on Figures 3(a) and 3(b), we can identify the onset of nondiffusive thermal transport to occur when the experimental length scale, $r_0$, becomes comparable to $\Lambda_e$ in a metal.

The characteristic length scale that defines the onset of electron-phonon nonequilibrium in a metal is $L_{noneq}$. When $r_0 > L_{noneq}$ in Figures 3(a) and 3(b), the electron and phonon thermal resistances are equivalent in both the BTE and diffusive models. As $r_0$ becomes commensurate to $L_{noneq}$ the electron and phonon thermal resistances separate. Therefore, when $r_0 >> L_{noneq}$ under low heat frequency conditions, $k_{exp}$ in a FDTR measurement will not be dependent on whether a two-temperature diffusive model or a single thermal energy carrier diffusive model is used to interpret the FDTR data. The parameters used to generate the thermal resistances as a function of $r_0$ in Figure 3 are shown in Table I.

Table I: Parameters used in the two-temperature diffusive and BTE models at 300 K and 25 K.

| | 300 K | 25 K |
|---|---|---|
| $k_e$ (W m$^{-1}$ K$^{-1}$) | 307 [27] | 977 [27] |
| $k_p$ (W m$^{-1}$ K$^{-1}$) | 3.3 [28] | 23 |
| $C_e$ (MJ m$^{-3}$ K$^{-1}$) | 0.021 [23] | 0.0017 [23] |
| $C_p$ (MJ m$^{-3}$ K$^{-1}$) | 2.50 [30] | 0.51 [30] |
| $g$ ($\times 10^{16}$ W m$^{-3}$ K$^{-1}$) | 3.0 [18] | 0.5 [18] |
| $v_e$ ($\times 10^{6}$ m s$^{-1}$) | 1.4 [31] | 1.4 [31] |
| $v_p$ (m s$^{-1}$) | 3240 [32] | 3240 [32] |
| $L_{th}$ (nm) | 101 | 442 |

## V. THERMAL CONDUCTIVITY SUPPRESSION FUNCTION

The thermal conductivity suppression function, $S$, predicts the apparent $k_{exp}$ in a FDTR experiment under nondiffusive thermal transport conditions [13]. When $R_{BTE} = R_{diff}$, the heat diffusion equation accurately predicts the thermal resistance at the surface and $k_{exp} = k_{bulk}$. Under nondiffusive conditions, $R_{BTE} > R_{diff}$ and $k_{exp} < k_{bulk}$.

The measured thermal resistance at the surface of the metal is a linear combination of $R_{BTE,e}$ and $R_{BTE,p}$ [35,36]. The thermal resistance probed at the surface can be expressed as $aR_{BTE,e} + bR_{BTE,p}$, where $a + b = 1$. Choi *et al* [19] found that $a/b = 0.02$ for Au at a laser beam wavelength of 785 nm. FDTR's probe laser beam has a wavelength of 532 nm, which is close to Au's interband transition threshold of 2.4 eV [37]. Fortunately, $S$ varied by less than 1% between the extremes of $a$ and $b$. Therefore, $a = 0$ and $b = 1$ was used to calculate $S$. To demonstrate that the chosen values of $a$ and $b$ do not change the conclusions of our work, Figure S1 in the Supplemental Materials [38] reproduces Figure 6 assuming $a = b = 0.5$.

To determine $S$ for a metal, an effective electronic thermal conductivity, $k_{e,eff}$, was found for each $r_0$ under the condition that $R_{BTE,p} = R_{diff,p}$. Only $k_e$ was varied, while $k_p$ remained constant, because electrons are the dominant source of $k$ in metals. The values of $k_{e,eff}$ were determined numerically because $k_{e,eff}$ could not be isolated analytically. The model presented here produces a $S$ that is identical to Regner *et al*'s [14] for highly coupled materials ($g \to \infty$).

The thermal conductivity suppression function, $S = k_{e,eff}/k_e$, is shown in Figure 4 for Au at temperatures of 300 K and 25 K. When $r_0 >> \Lambda_e$ the thermal transport is purely diffusive and $S = k_{e,eff}/k_e = 1$. As $r_0$ decreases and becomes commensurate to $\Lambda_e$, $R_{BTE,p} > R_{diff,p}$ and $S < 1$. Notably, $S$ is independent of the value of $L_{th}$ used to determine the isothermal region thickness, except in its influence on $\varepsilon_e$.

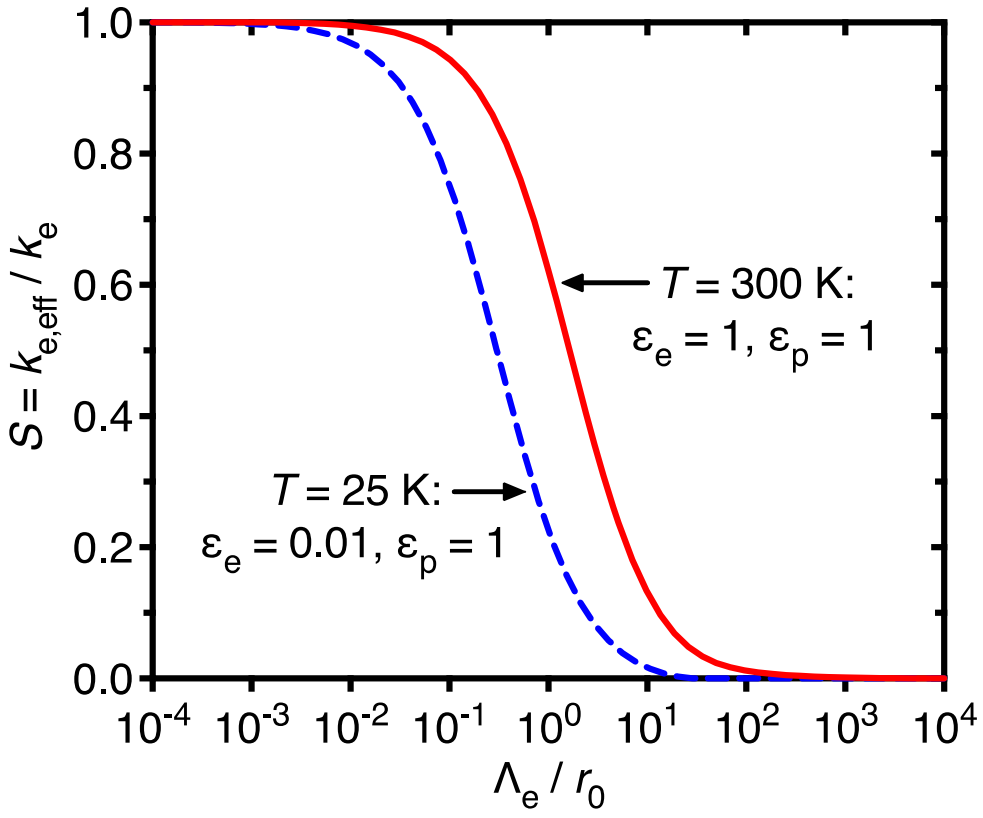


FIG. 4. $S$ for a bulk Au crystal measured via FDTR at temperatures of 300 K and 25 K under low heating frequency conditions. When $r_0 >> \Lambda_e$, $S = 1$ because the transport is purely diffusive. As $r_0$ becomes similar to $\Lambda_e$ the electrons transport nondiffusively and $S < 1$. $S$ results a broad distribution of $k_{e,eff}$ over a wide range of $r_0$, despite the narrow distribution of $k_{accum}$ for electrons in a metal.

## VI. EXPERIMENTAL RESULTS

To test the theoretically derived $S$, $k_{exp}$ of a bulk Au crystal (99.999% Au, 10 mm radius by 1 mm thickness, (100) orientation) was measured via FDTR at 304 K, 35 K, 28 K, and 23 K. The values of $L_{th}$, $C_e$ , $C_p$, and $g$ used for extracting $k_{exp}$ are listed in Table II. Based on the absorbed laser powers the temperature rises due to steady state laser

heating have been accounted for in the reported temperatures (typically less than 5 K added to the base cryostat temperature). Periodic oscillations in temperature were less than 2 K for all measurements.

Table II: Values of $L_{th}$, $C_e$ , $C_p$, and $g$ used in the diffusive model to extract $k_{exp}$.

| | 304 K | 35 K | 28 K | 23 K |
|---|---|---|---|---|
| $L_{th}$ (nm) | 101 | 239 | 343 | 526 |
| $C_e$ (MJ m$^{-3}$ K$^{-1}$) | 0.021 [23] | 0.0024 [23] | 0.0019 [23] | 0.0016 [23] |
| $C_p$ (MJ m$^{-3}$ K$^{-1}$) | 2.45 [30] | 0.92 [30] | 0.64 [30] | 0.43 [30] |
| $g$ ($\times 10^{16}$ W m$^{-3}$ K$^{-}$ | 3.0 [19] | 1.0 [18] | 0.68 [18] | 0.41 [18] |

The FDTR phase-lag vs. heating frequency data was fit to the electron-phonon coupled heat diffusion equations in cylindrical coordinates, as outlined by Wilson *et al* [39], with the additional ability for non-surface heat deposition [40]. This two-temperature model was chosen for thoroughness, but we note that a one-temperature model with the same non-surface heat deposition length scale [41], results in identical values of $k_{exp}$. This result is consistent with the disparity in timescales between the electron-phonon coupling timescales (< 1ps [17]) and the timescales (0.2 μs and 10 μs) of the chosen FDTR frequencies, as well as the length scales driving nonequilibrium $L_{noneq}$ (Fig. 3), which are far smaller than the chosen values of $r_0$.

In the two-temperature model, electrons absorb heat from the pump laser beam and exponentially deposit heat into the lattice over the length scale $L_{th}$ [21,42]. To mimic exponential heat deposition in our diffusive model, the bulk Au sample was divided into 14 different layers. The first 13 layers (from the surface of the Au to a depth of $3L_{th}$) each had a thickness of $\frac{3L_{th}}{13}$ and the 14$^{th}$ unheated layer had a thickness of 1 mm, where no

thermal resistance existed between each layer. In the middle of the first 13 layers different percentages of the absorbed laser heat flux were deposited, as shown in Figure 5(a). The heat was deposited over $3L_{th}$ to ensure that roughly all of the heat was deposited in an exponential manner.

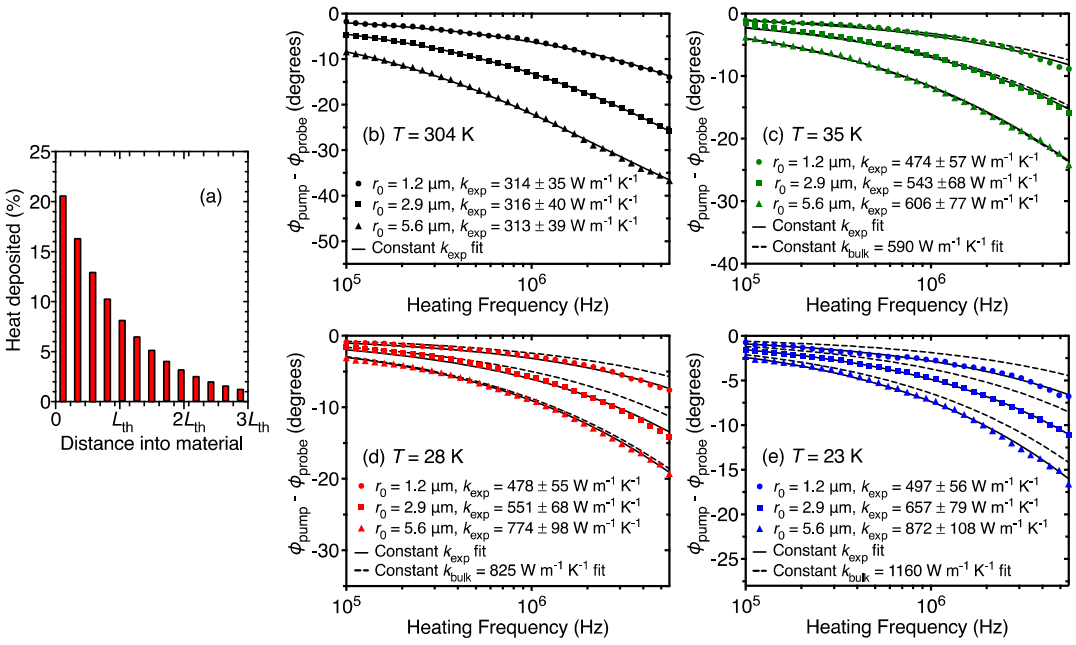


FIG. 5. (a) Percentage of the total absorbed laser heat flux deposited into the first 13 surface layers of the bulk Au crystal over the length $3L_{th}$ in the diffusive model used to fit the FDTR phase-lag vs. heating frequency data. (b)-(e) FDTR phase-lag vs. heating frequency data for a bulk Au crystal measured at (b) 304 K, (c) 35 K, (d) 28 K, and (e) 23 K. No heating frequency dependence on $k_{exp}$ was observed at all four temperatures and no $r_0$-dependence on $k_{exp}$ was observed at 304 K.

The phonon temperature at one optical penetration depth from the surface of the Au (18 nm based on the probe laser beam's wavelength [43]) was fit to the measured FDTR

phase-lag data. One optical penetration depth was chosen, as opposed to the surface temperature, because Au's thermoreflectance signal is a result of probe laser photons that are reflected volumetrically over the optical penetration depth. The values of $k_{exp}$ are however insensitive to the depth at which the temperature was fit between the surface and two optical penetration depths. The fitted $k_{exp}$ represents the total thermal conductivity of the electrons and the phonons.

The FDTR phase-lag vs. heating frequency data for a bulk Au crystal measured at 304 K is shown in Figure 5(b). Using the diffusive model described above, no heating frequency or $r_0$-dependence on $k_{exp}$ was observed at 304 K. The laser spot size radii were $r_0$ = 1.2 μm, 2.9 μm, and 5.6 μm, measured using the knife-edge technique. The bulk value of thermal conductivity at 304 K (310 W m$^{-1}$ K$^{-1}$ [27]) fit the phase-lag vs. heating frequency data across all three $r_0$'s. The bulk value of $k$ was measured at 304 K because $r_0$ and $L_P$ were much greater than the MFPs of the electrons and phonons.

To verify that the absorbed laser heat flux must be deposited exponentially over $L_{th}$, a sensitivity analysis of heat deposition was conducted for the FDTR data at 304 K. When the laser heat flux was deposited exponentially over $L_e$, $\Lambda_e$, and the optical penetration depth ( $\delta$ ) of the pump laser beam, $k_{exp}$ was found to be $r_0$-dependent. The $k_{exp}$ values when the heat flux was exponentially deposited over all four length scales are shown in Table III for the three $r_0$. Only $L_{th}$ defined analytically as $\sqrt{k_e / g}$ results in $k_{exp} = k_{bulk}$ at 304 K, thus supporting its choice over these alternative length scales. Another possible interpretation of our experimental results would be to fit the measured phase-lag vs. heating frequency data assuming $k_{exp} = k_{bulk}$ to identify the length scale of heat deposition. The results of this analysis are shown in Table IV. At 304 K, $L_{th}$ is ~100 nm

across all three spot size radii, while $L_{th}$ is $r_0$-dependent at 35 K, 28 K, and 23 K. Still another possibility is that electron transport in the radial direction would enlarge the effective $r_0$ for heat deposition, but we did not explore this approach because it was inconsistent with our data at 304 K. Hence, since it is unclear why $L_{th}$ would depend on $r_0$ the most reasonable interpretation of our data is to use an $r_0$-dependent $k_{exp}$ where the heat deposition length scale is $L_{th} = \sqrt{k_e / g}$.

Table III: Values of $k_{exp}$ (W m$^{-1}$ K$^{-1}$) at 304 K using different exponential heat deposition lengths.

| Heat deposition length | $r_0 = 1.2\ \mu$m | $r_0 = 2.9\ \mu$m | $r_0 = 5.6\ \mu$m |
|---|---|---|---|
| $L_{th}$ (101 nm) | 314 | 315 | 319 |
| $L_e$ (10 nm) | 266 | 286 | 295 |
| $\Lambda_e$ (31 nm) | 276 | 292 | 300 |
| $\delta$ (21 nm) | 271 | 289 | 298 |

Table IV: Values of $L_{th}$ (nm) needed to fit FDTR data to $k_{exp} = k_{bulk}$

| Temperature | $r_0 = 1.2$ μm | $r_0 = 2.9$ μm | $r_0 = 5.6$ μm |
|---|---|---|---|
| 304 K | 100 | 100 | 101 |
| 35 K | 427 | 365 | 193 |
| 28 K | 1066 | 966 | 498 |
| 23 K | 1880 | 1800 | 1320 |

The FDTR phase-lag vs. heating frequency data at temperatures of 35 K, 28 K, and 23 K are shown in Figures 5(c), 5(d), and 5(e), respectively. At 35 K, $k_{exp} = k_{bulk}$ for the two larger spot sizes, $r_0 = 2.9$ and 5.6 μm, while $k_{exp} = 0.8k_{bulk}$ at 35 K when $r_0 = 1.2$ μm.

At 28 K and 23 K, $k_{exp} < k_{bulk}$ because $\Lambda_e \sim 0.9$ μm and 1.6 μm, respectively, which are similar to the $r_0$'s used in the FDTR experiment (at 23 K, $\Lambda_e$ is greater than the smallest $r_0$ = 1.2 μm). Therefore, the electrons exhibited nondiffusive thermal transport and a suppressed from bulk value of $k$ was measured for all $r_0$. Figures 5(c), 5(d), and 5(e) include the predicted phase-lag vs. heating frequency for $k_{bulk}$ to demonstrate the measured phase-lag deviation from $k_{bulk}$.

Figure 6 shows $k_{accum}(\Lambda_e^*)$, the predicted $k_{exp}$ based on $S$, and the measured $k_{exp}$. The predicted values of $k_{exp}$ are based on Equation (3), where $k_{exp}\left(r_0\right) = S\left(\Lambda_e, r_0\right)k_e$. Regner *et al* [14] found that predicted values of $k_{exp}$, based on $S$, matched experimental values of $k_{exp}$ when a $r_0$ three times greater than the experimental value was used in $S$. The authors argued that the geometric factor of three accounted for the fact that $S$ was based on a spherical model that only approximately captured surface heating in a finite Gaussian distribution. Since a rigorously defined geometric factor that accounts for the difference in spherical vs. cylindrical heating is uncertain, we have plotted the predicted $k_{exp}$ as a band, where a value of $3r_0$ substituted into $S$ is the left-most dashed line and a value of $r_0$ substituted into $S$ is the right-most dashed line.

The y-axis in Figure 6 is normalized by $k_{bulk}$ for each temperature. The predicted $k_{exp}$ and the measured $k_{exp}$ agree favorably across all four temperatures. The size of the error bars were determined by independently varying $C_e$, $C_p$, $g$, $L_{th}$, and $r_0$, shown in Table II, by ± 6% in the heat diffusion model used to extract $k_{exp}$ [44]. At 304 K, $k_{exp} = k_{bulk}$, because the thermal transport is purely diffusive, as predicted by $S$. At 35 K, the values of $k_{exp}$ as a function of $r_0$ varied between 103% and 80% of $k_{bulk}$, while the values of $k_{exp}$ at 28 K and 23 K varied between 94% to 58% of $k_{bulk}$ and 75% to 43% of $k_{bulk}$, respectively.

Although some phonons may have MFPs greater than $r_0$ at 28 K and 23 K, they make only small contributions to thermal conductivity. Hence, we conclude that nondiffusive electron transport dominates suppression in $k$. This demonstrates that even when a gray $\Lambda_e$ exists, $k_{exp}$ can exhibit a broad distribution of values as a function of FDTR's characteristic length scales.

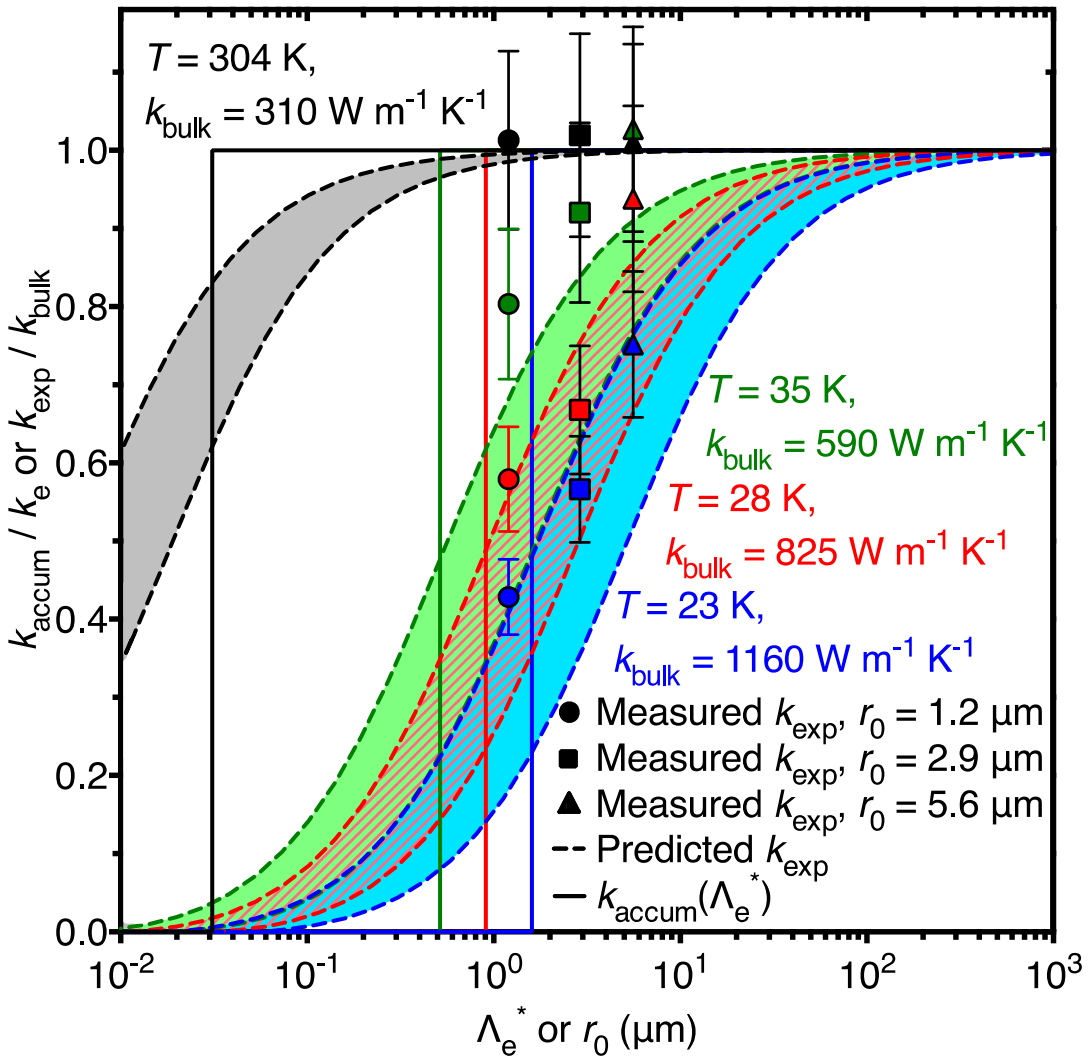

FIG. 6. Measured $k_{exp}$, predicted $k_{exp}$, and $k_{accum}(\Lambda_e^*)$ for a bulk Au crystal at 304 K, 35 K, 28 K, and 23 K. The predicted $k_{exp}$ are plotted as bands to account for the geometric uncertainty of spherical vs. cylindrical heating. At 304 K, the bulk value of thermal conductivity was measured with all three $r_0$, while $k_{exp}$ was $r_0$-dependent at 35 K, 28 K, and 23 K. The measured values of $k_{exp}$ matched the predicted values of $k_{exp}$, based on $S$, favorably at all four temperatures.

## VII. CONCLUSION

In this work we developed an analytical $S$ for a coupled energy carrier system and demonstrated its ability to accurately predict $k_{exp}$ as a function of $r_0$ in a FDTR experiment. This study provides the most extreme example of $k_{exp}$ broadening due to $S$ because of the gray $\Lambda_e$ in metals. In nondiffusive, coupled energy carrier materials, it is essential to separate nonequilibrium transport effects from nondiffusive effects and the length scales and/or time scales associated with the two transport processes. Our theoretical model now provides a roadmap for describing nanoscale thermal transport in metals and many other types of coupled systems, such as phonon-magnon [45-47] and low frequency ballistic-high frequency diffusive phonon systems [39], where nonequilibrium and nondiffusive transport may coexist.

## ACKNOWLEDGMENTS

We thank Alan J. H. McGaughey and Keith T. Regner for helpful discussions and the NSF CBET Award #1133394 and the Natural Science and Engineering Research Council of Canada for funding.

[[1] K. T. Regner, D. P. Sellan, Z. Su, C. H. Amon, A. J. H. McGaughey, and J. A. Malen, Nat. Commun. **4**, 1640 (2013).
[2] J. P. Freedman, J. H. Leach, E. A. Preble, Z. Sitar, R. F. Davis, and J. A. Malen, Sci. Rep. **3**, 2963 (2013).
[3] J. A. Johnson, A. A. Maznev, J. Cuffe, J. K. Eliason, A. J. Minnich, T. Kehoe, C. M. Sotomayor Torres, G. Chen, and K. A. Nelson, Phys. Rev. Lett. **110**, 025901 (2013).
[4] Y. K. Koh and D. G. Cahill, Phys. Rev. B **76**, 075207 (2007).
[5] A. J. Minnich, J. A. Johnson, A. J. Schmidt, K. Esfarjani, M. S. Dresselhaus, K. A. Nelson, and G. Chen, Phys. Rev. Lett. **107**, 095901 (2011).
[6] D. Ding, X. Chen, and A. J. Minnich, Appl. Phys. Lett. **104**, 143104 (2014).
[7] G. Chen, *Nanoscale Energy Transport and Conversion: A Parallel Treatment of Electrons, Molecules, Phonons, and Photons* (Oxford University Press, New York, 2005).
[8] G. Tas and H. J. Maris, Phys. Rev. B **49**, 15046 (1994).
[9] T. Q. Qiu and C. L. Tien, Int. J. Heat Mass. Tran. **35**, 719 (1992).
[10] T. Q. Qiu and C. L. Tien, J. Heat Trans. **115**, 842 (1993).
[11] T. Q. Qiu and C. L. Tien, J. Heat Trans. **115**, 835 (1993).
[12] C. Dames and G. Chen, in *Thermoelectrics Handbook: Macro to Nano*, edited by D. M. Rowe (CRC Press, Boca Raton, FL, 2006), pp. 42.1-42.16.
[13] A. J. Minnich, Phys. Rev. Lett. **109**, 205901 (2012).
[14] K. T. Regner, A. J. H. McGaughey, and J. A. Malen, Phys. Rev. B **90**, 064302 (2014).
[15] A. A. Maznev, J. A. Johnson, and K. A. Nelson, Phys. Rev. B **84**, 195206 (2011).
[16] K. C. Collins, A. A. Maznev, Z. Tian, K. Esfarjani, K. A. Nelson, and G. Chen, J. Appl. Phys. **114**, 104302 (2013).
[17] R. H. M. Groeneveld, R. Sprik, and A. Lagendijk, Phys. Rev. B **51**, 11433 (1995).
[18] W. Wang and D. G. Cahill, Phys. Rev. Lett. **109**, 175503 (2012).
[19] G. M. Choi, R. B. Wilson, and D. G. Cahill, Phys. Rev. B **89**, 064307 (2014).
[20] M. I. Kaganov, I. M. Lifshitz, and L. V. Tanatarov, Sov. Phys. JETP **4**, 173 (1957).
[21] S. D. Brorson, J. G. Fujimoto, and E. P. Ippen, Phys. Rev. Lett. **59**, 1962 (1987).
[22] A. Pattamatta and C. K. Madnia, J. Heat Trans. **131**, 082401 (2009).
[23] Z. Lin, L. V. Zhigilei, and V. Celli, Phys. Rev. B **77**, 075133 (2008).
[24] H. E. Elsayed-Ali, T. B. Norris, M. A. Pessot, and G. A. Mourou, Phys. Rev. Lett. **58**, 1212 (1987).
[25] M. F. Modest, *Radiative Heat Transfer* (Academic Press, San Diego, CA, 1993).
[26] G. Chen, J. Heat Trans. **118**, 539 (1996).

[27] C. Y. Ho, R. W. Powell, and P. E. Liley, J. Phys. Chem. Ref. Data **1**, 279 (1972).
[28] J. G. Cook and M. P. van der Meer, Can. J. Phys. **48**, 254 (1970).
[29] F. Yang and C. Dames, Phys. Rev. B **87**, 035437 (2013).
[30] G. T. Furukawa, W. G. Saba, and M. L. Reilly, *Critical Analysis of the Heat Capacity Data of the Literature and Evaluation of Thermodynamic Properties of Copper, Silver, and Gold from 0 to 300 K* (National Bureau of Standards, Washington, DC, 1968).
[31] N. W. Ashcroft and N. D. Mermin, *Solid state physics* (Holt, New York, NY, 1976).
[32] J. W. Lynn, H. G. Smith, and R. M. Nicklow, Phys. Rev. B **8**, 3493 (1973).
[33] R. A. Matula, J. Phys. Chem. Ref. Data **8**, 1147 (1979).
[34] T. Q. Qiu and C. L. Tien, Int. J. Heat Mass Tran. **37**, 2789 (1994).
[35] P. M. Norris, A. P. Caffrey, R. J. Stevens, J. M. Klopf, J. T. McLeskey, and A. N. Smith, Rev. Sci. Instrum. **74**, 400 (2003).
[36] S. D. Brorson, A. Kazeroonian, J. S. Moodera, D. W. Face, T. K. Cheng, E. P. Ippen, M. S. Dresselhaus, and G. Dresselhaus, Phys. Rev. Lett. **64**, 2172 (1990).
[37] W. J. Scouler, Phys. Rev. Lett. **18**, 445 (1967).
[38] See Supplemental Materials at [] for a figure reproducing Figure 6 assuming $a = b = 0.5$.
[39] R. B. Wilson, J. P. Feser, G. T. Hohensee, and D. G. Cahill, Phys. Rev. B **88**, 144305 (2013).
[40] K. T. Regner, L. C. Wei, and J. A. Malen, J. Appl. Phys. **118**, 235101 (2015).
[41] J. Yang, E. Ziade, and A. J. Schmidt, J. Appl. Phys. **119**, 095107 (2016).
[42] M. Battiato, K. Carva, and P. M. Oppeneer, Phys. Rev. B **86**, 024404 (2012).
[43] G. Joos and A. Klopfer, Z. Phys. **138**, 251 (1954).
[44] J. A. Malen, K. Baheti, T. Tong, Y. Zhao, J. A. Hudgings, and A. Majumdar, J. Heat Trans. **133**, 081601 (2011).
[45] G. T. Hohensee, R. B. Wilson, J. P. Feser, and D. G. Cahill, Phys. Rev. B **89**, 024422 (2014).
[46] M. C. Langner, C. L. S. Kantner, Y. H. Chu, L. M. Martin, P. Yu, R. Ramesh, and J. Orenstein, Phys. Rev. B **82**, 054425 (2010).
[47] B. L. Liao, J. W. Zhou, and G. Chen, Phys. Rev. Lett. **113**, 025903 (2014).